PHOTONICS Research

Microcrystal modulated exciton-polariton emissions from single ZnO@ZnO:Ga microwire

Wangqi Mao,[1] Mingming Jiang,[1,2,*] Jiaolong Ji,[1] Peng Wan,[1] Xiangbo Zhou,[1] and Caixia Kan[1,2,3]

[1]College of Science, Nanjing University of Aeronautics and Astronautics, Nanjing 210016, China
[2]Key Laboratory for Intelligent Nano Materials and Devices (MOE), Nanjing University of Aeronautics and Astronautics, Nanjing 210016, China
[3]e-mail: cxkan@nuaa.edu.cn
*Corresponding author: mmjiang@nuaa.edu.cn

Received 30 July 2019; revised 15 October 2019; accepted 25 November 2019; posted 27 November 2019 (Doc. ID 374101); published 31 January 2020

Due to their outstanding surface-to-volume ratio, highly smooth surface, and well-defined crystal boundary, semiconducting micro-/nanocrystals have been used as a pivotal platform to fabricate multifunctional optoelectronic devices, such as superresolution imaging devices, solar concentrators, photodetectors, light-emitting diodes (LEDs), and lasers. In particular, micro-/nanocrystals as key elements can be employed to tailor the fundamental optical and electronic transport properties of integrated hetero-/homostructures. Herein, ZnO microcrystal-decorated pre-synthesized Ga-doped ZnO microwire (ZnO@ZnO:Ga MW) was prepared. The single ZnO@ZnO:Ga MW can be used to construct optically pumped Fabry–Perot (F–P) mode microlasers, with the dominating lasing peaks centered in the violet spectral region. Stabilized exciton-polariton emissions from single ZnO@ZnO:Ga MW-based heterojunction diode can also be realized. The deposited ZnO microcrystals can facilitate the strong coupling of F–P optical modes with excitons, leading to the formation of exciton-polariton features in the ZnO@ZnO:Ga MW. Therefore, the waveguiding lighting behavior and energy-band alignment of ZnO microcrystal-sheathed ZnO:Ga MW radial structures should be extremely attractive for potential applications in semiconducting microstructure-based optoelectronic devices, such as micro-LEDs, laser microcavities, waveguides, and photodetectors.

https://doi.org/10.1364/PRJ.8.000175

1. INTRODUCTION

Owing to high photostability, controlled sizes, and wide spectral tunability, semiconducting low-dimensional crystals are attractive for their superiority and widespread application prospects in illumination and displays, lasers, fluorescence tagging, and so on [1–5]. Tremendous effort and progress have been made to investigate the synthesis of low-dimensional crystals, together with micro-/nanocrystal modulated optical cavities. The incorporation of low-dimensional crystals has been used to achieve surface passivation of semiconducting structures. Additionally, the deposition of these crystals can also be functionalized relatively easily to enable not only their grafting to other molecules but also their colloidal dispersion in various solvents [6–10]. Thus, by adjusting the size and surface morphology of the as-synthesized low-dimensional crystals, optical and electronic properties can be modulated, which represents an enormous challenge in the application of the fabrication of novel functional devices [11–13]. Micro-/nanocrystals serving as optical gain materials have been prepared using chemical vapor transport, hydrothermal method, molecular beam epitaxy, lithographically induced self-assembly, etc. Although various attempts have been made to fabricate large-sized crystals with controlled size and morphologies, it is still a significant challenge to prepare complex structures with controlled crystalline morphology, orientation, and surface architecture [14–16]. Therefore, the fabrication of semiconducting crystals with various sizes and special morphologies, as well as the application of low-dimensional crystals as optically active units, has become problems that require quick resolution [17–19].

Furthermore, semiconductor micro-/nanocrystals as design elements have been employed for surface modification as well as the modulation of band structure to make it responsive for desired purposes [20–23]. In particular, due to their unique advantages of light absorption, light emission, and electron transfer, it has been reported that semiconducting micro-/nanocrystal-based hetero-/homostructures have acquired remarkable attention for fabricating different photonic and optoelectronic devices, such as microsized light-emitting diodes (LEDs) and lasers, photoelectric detectors, and photovoltaics [24–27]. Because of its direct wide bandgap of 3.37 eV and 60 meV of exciton-binding energy at room temperature, zinc oxide (ZnO) has widespread application in photonic and optoelectronic devices, photocatalyst and photovoltaic devices,

transparent electrodes, gas sensors, biosensors, and so on. The outstanding optical and electrical properties of ZnO-based materials are highly dependent on the surface morphologies and crystalline structures. For instance, ZnO-based micro-/nanocrystals, possessing the high crystalline quality derived from its remarkable surface-to-volume ratio, have already attracted extensive attention and applications in the design of novel optoelectronic devices [4,28–32]. Various routes have been developed to synthesize ZnO micro-/nanostructures. A simple and efficient experimental way to prepare mass and well-crystallized ZnO micro-/nanocrystals, including for the fabrication of optoelectronic devices combining semiconducting structures and ZnO low-dimensional crystal-based coating, is necessary [19,33,34].

In this context, ZnO microcrystals (MCs) were successfully synthesized and can be used to construct optically pumped random lasing. Interestingly, ZnO MCs can also be deposited on the pre-synthesized Ga-doped ZnO microwires (ZnO@ZnO:Ga MWs) using two-step carbothermal reduction methods. The as-synthesized single ZnO@ZnO:Ga MW features a well-defined quadrilateral shape. To exploit the influence of ZnO MCs on the optical properties of single ZnO:Ga MW, optically pumped violet Fabry–Perot (F–P) mode lasing was achieved from single ZnO@ZnO:Ga MW. The redshift of the lasing band may be assigned to the type-II band alignment. A heterojunction diode composed of a single ZnO@ZnO:Ga MW and p-GaN layer was also constructed. The observed series of resonance peaks on the electroluminescence (EL) spectra could be ascribed to the exciton-polariton emission. Thus, single ZnO@ZnO:Ga MW can provide a candidate to achieve strong coupling of optical modes with excitons, leading to the formation of exciton-polaritons, and single ZnO@ZnO:Ga MW can afford essential prerequisites to construct a real-world electrical injection exciton-polariton diode. These experimental findings represent a major advancement for the design and synthesis of ZnO-based homo-/heterostructure-based exciton-polariton diodes and multicolor light sources. This also paves the way toward future integrated photonic and optoelectronic devices with superior performance.

2. EXPERIMENTAL SECTION

A. Synthesis of Individual ZnO@ZnO:Ga MWs

By means of a simple carbothermal reduction method, ZnO MCs were successfully synthesized. Compared with the synthesis of ZnO micro-/nanowires, higher growing temperature (1100°C) and hypoxic growth environment should be taken into account [33,35,36]. ZnO MCs can also be deposited on the pre-synthesized ZnO:Ga MW using two-step chemical vapor deposition (CVD). A horizontal alundum tube reactor with double-engineered reaction temperature gradient zones was adopted in the synthesized procedure [28,29,36]. A corundum boat with a mixture of high-purity powders with the weight ratio of ZnO:graphite C = 1:1 served as the precursor reaction source and was placed in the high-temperature zone (**I**), which was located upstream of the carrier gas (growth temperature: 1100°C). The other corundum boat with the precursor of high-purity mixed powders with the weight ratio of ZnO:Ga_2O_3:C = 10:1:11 was placed in the other high-temperature zone (**II**), which was located downstream (growth temperature: 1150°C), accompanied by cleaned Si (100) substrates (without any catalyst coating) placed on the corundum boat to collect the products. During the synthesis process, a constant flow of argon (Ar) (99.99%) (200 sccm), which served as the protecting gas, was introduced into the furnace chamber. The synthesis procedure is summarized as follows. First, the reaction zone **II** should be heated up to 1150°C and maintained 30 min; thus, individual ZnO:Ga MWs can be collected around the Si substrate. Second, after individual ZnO:Ga MWs have been collected, the reaction zone **I** should be raised up to the growth temperature at 1100°C as soon as possible. Driven by carrier gas (Ar), the thermal evaporated Zn vapor will accumulate around the pre-synthesized ZnO:Ga MWs. Third, incorporated with residual oxygen (O_2) in the horizontal furnace chamber, ZnO MCs will be deposited on the MWs. After maintaining the hypoxia-synthesis condition 30 min, 20% O_2 should be introduced into the tube furnaces. Individual ZnO:Ga MWs covered with ZnO MC decoration can be collected around the Si wafer in the downstream reaction temperature zone **II**. By adjusting the synthesis parameters—such as the ratio of the precursor mixtures—the reaction time as well as the reaction temperatures, the size and surface morphology of ZnO MCs, and the ZnO MC concentration deposited on the pre-synthesized ZnO:Ga MWs can be modulated.

B. Fabrication of Heterojunction Diode Composed of Single ZnO@ZnO:Ga MW and p-GaN Layer

First, an insulating layer (such as MgO) was evaporated on the pre-cleaned p-GaN layer using molecular beam epitaxy. Second, Au and Ni/Au electrode was evaporated on the GaN layer using the electron-beam evaporation system. Third, single ZnO@ZnO:Ga MW was transferred across the boundary between the insulating layer and the p-GaN layer, accompanied by the In particle that served as the electrode and was fixed on the ZnO@ZnO:Ga MW, located on the insulating layer. Thus, a heterojunction diode composed of a single ZnO@ZnO:Ga MW and p-GaN layer was fabricated [28,30,37].

C. Analysis Instruments

The synthesized ZnO MCs and ZnO:Ga MWs as well as the single ZnO@ZnO:Ga MW were characterized using a scanning electron microscope (SEM). Room-temperature photoluminescence (PL) measurements of ZnO MCs, ZnO:Ga MWs, and ZnO@ZnO:Ga MWs were carried out using a He-Cd laser (excitation wavelength: 325 nm) via a LABRAM-UV Jobin Yvon spectrometer. Meanwhile, optically pumped lasing measurements of ZnO MCs and ZnO@ZnO:Ga MWs were also implemented. The excitation laser (λ_{ex} = 355 nm, repetition rate 1 kHz, pulse length 150 fs) was generated by an optical parametric amplifier (OPERA SOLO) from a Ti:sapphire laser (Coherent) and then focused onto the MWs through a confocal micro-PL system (Olympus BX53). A spectrometer (SpectraPro-2500i, Acton Research Corporation) was equipped to collect and analyze the optical spectrum. The electronic transport properties with current–voltage (*I–V*) characteristics curves were investigated using a Keithley 2611 system.

Light-emitting characteristics from an electrically driven single ZnO@ZnO:Ga MW-based heterojunction diode were measured, and the emission spectra were collected using a Hitachi F-7000 spectrometer. Optical microscope images of the heterojunction diode were also recorded using an optical microscope.

3. RESULTS AND DISCUSSION

A. Synthesis of Individual ZnO@ZnO:Ga MWs

Individual ZnO@ZnO:Ga MWs were synthesized using two-step CVD methods. The synthesis procedure is schematically illustrated in Fig. 1(a). The growth procedure is proposed as follows. First, individual ZnO:Ga MWs were prepared via carbon thermal reduction in the high-temperature zone (**II**) in advance. Afterward, temperature rising of zone **I** was started, and it reached the growing temperature of 1100°C right away. The Zn vapor began to appear and then gathered around the pre-synthesized ZnO:Ga MWs, driven by carrier gas. More and more Zn vapor started to adhere to the pre-synthesized MWs, which were reoxidized to form isolated ZnO MCs. Thereby, ZnO MCs can be synthesized and deposited on the pre-synthesized ZnO:Ga MWs. Figure 1(b) displays an optical photograph of the as-synthesized ZnO@ZnO:Ga MWs. It indicates that a mass of MWs can be collected around the Si substrate as well as the wall of the alundum boat [28,29]. Figure 1(c) illustrates the SEM image of the as-synthesized ZnO:Ga MWs, which possessed highly smooth surfaces, accompanied by the quadrilateral cross section displayed in the inset. In contrast, single ZnO@ZnO:Ga MW was also characterized, as shown in Fig. 1(d). Additionally, amplified SEM images of the synthesized ZnO MCs, which deposited on the ZnO:Ga MWs, were also characterized and are shown in Figs. 1(e)–1(g). By adjusting the growth conditions, ZnO MCs with controlled sizes and structural morphologies that deposited on the pre-synthesized MWs can be modulated.

B. Optically Pumped Random Lasing of Single ZnO MC

To illustrate the influence of ZnO MCs on the optical properties of single ZnO:Ga MW, a single ZnO MC was selected, as shown in Fig. 2(a). The optical characterization of the selected ZnO MC was excited by a 355 nm fs laser under the confocal micro-PL system. Increasing the excitation energy density per pulse I_{exc} ranging from 9 to 12 mW/μm^2, optical micrographs of ultraviolet emission were recorded, as shown in Fig. 2(b). The micro-PL spectra from the selected ZnO MC as a function of the I_{exc} were also recorded. Taking the $I_{exc} \sim 10.0$ mW/μm^2 as an example, a series of sharp emission peaks appeared on the broad emission spectrum. That is, five emission peaks with the average spectral linewidth of 0.18 nm appeared, with the peak positioned at 390.22, 391.04, 391.94, 392.88, and 393.73 nm, which indicates that optical resonance with specific modes was formed in the ZnO MC. The Q factor of this microcavity was calculated to be about 2000 according to the equation $Q = \lambda/\delta\lambda$, where λ and $\delta\lambda$ are the dominant lighting peak wavelength and the spectral linewidth, respectively. With an increase in I_{exc}, the sharp lighting peaks became greater, and the lighting intensity increased dramatically. The emission spectra versus the I_{exc} were also collected, as exhibited

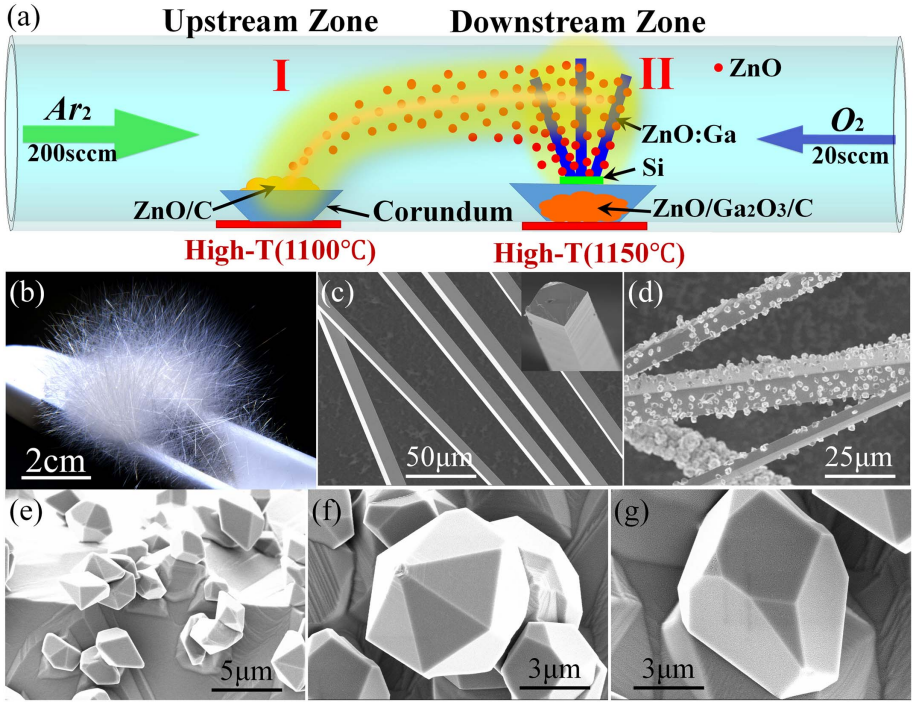

Fig. 1. Synthesis of single ZnO@ZnO:Ga MW. (a) Schematic diagram of the preparation procedure of ZnO MC-decorated pre-synthesized ZnO:Ga MWs. (b) Optical photograph of the as-synthesized individual ZnO@ZnO:Ga MWs, located around the Si substrate. (c) SEM image of the pre-synthesized ZnO:Ga MWs, with perfect quadrilateral cross section displayed in the inset. (d) SEM image of the as-synthesized individual ZnO@ZnO:Ga MWs. (e)–(g) Amplified SEM image of ZnO MCs, deposited on the ZnO:Ga MWs.

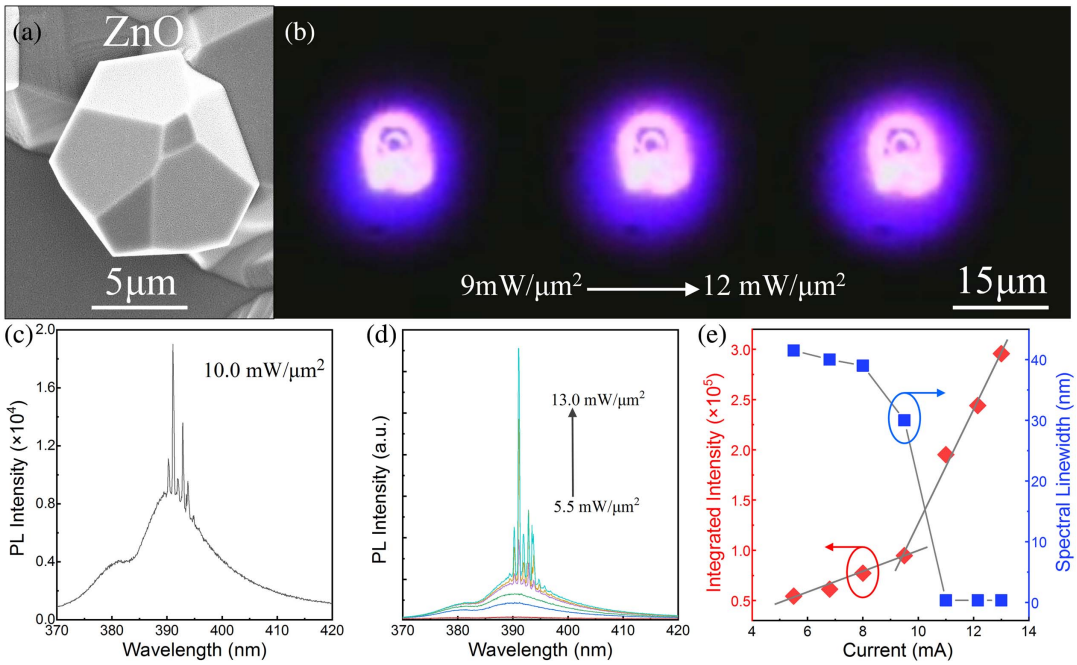

Fig. 2. Optically pumped random lasing features from single ZnO MC. (a) SEM image of as-synthesized single ZnO MC. (b) Microscopic images of light emission from optically pumped single ZnO MC, with the excitation power density ranging from 9.0 to 12.0 mW/μm^2. (c) Optically pumped lasing spectrum from single ZnO MC, with the excitation power density of 10 mW/μm^2. (d) Optically pumped emission spectra from single ZnO MC, with the excitation power densities ranging from 5.5 to 13.0 mW/μm^2. (e) Nonlinear relationship of integrated emission intensities as a function of the excitation power density, together with the spectral linewidth versus the excitation power density. The lasing threshold was extracted to be about 10.3 mW/μm^2.

in Fig. 2(d). This figure illustrates that when the I_{exc} was below 7.5 mW/μm^2, a single broad emission peak centered at 390 nm was observed, which can be attributed to typical near-band emission (NBE) of ZnO-based materials [19,28,33,38,39]. When the I_{exc} was beyond 9.0 mW/μm^2, a turning point could be obtained between two different linear regions, with a kink point at the pumping power density of about 10.2 mW/μm^2, as shown in Fig. 2(e).

To exploit the lighting features, when the I_{exc} was beyond 10.5 mW/μm^2, the emission spectra were dominated by sharp emission lines, and more and more emission peaks appeared with the increase of I_{exc}. Thus, the emission intensity from single ZnO MC exhibited a dramatically superlinear increase, yielding orders of magnitude greater than the spontaneous emission background. This indicated that multi-mode lasing action was generated in the single ZnO MC. One prominent lasing behavior was that the spectral linewidth of the light emission band was narrowing from 12.5 to 0.15 nm. The integrated emission intensity as a function of the pumping power density is depicted in Fig. 2(e). The output-input curve agrees well with the Casperson model for multi-mode laser. The critical pumping power density of 10.5 mW/μm^2 was estimated as the lasing threshold. Therefore, optically pumped lasing action was realized from a single ZnO MC. To distinguish the lasing characteristics, the observed lighting peaks cannot be attributed to the typical whispering gallery mode (WGM) resonator as well as the F–P mode resonator. Therefore, optically pumped random lasing was realized on account of the as-synthesized ZnO MCs [8,30,31,33,34].

C. Optically Pumped Fabry–Perot Mode Lasing of Single ZnO@ZnO:Ga MW

The influence of ZnO MCs on the optical properties of the pre-synthesized ZnO:Ga MWs was taken into account. Figure 3(a) displays the PL spectrum of single ZnO@ZnO:Ga MW, with the $I_{exc} \sim 7.0$ mW/μm^2. There were two dominating emission peaks centered around 380 and 395 nm in the ultraviolet spectral region. Increasing the I_{exc} ranging from 3.0 to 9.0 mW/μm^2, the micro-PL spectra showed that ultraviolet NBE-type spontaneous emissions can be obtained, as displayed in Fig. 3(b). Taking the I_{exc} as 3.0 mW/μm^2, for instance, the dominant emission wavelength centered at 379.5 nm with a spectral linewidth of about 12 nm was captured. When the I_{exc} increased to 7.0 mW/μm^2, two emission peaks centered at 381.5 and 395.4 nm appeared on the broad emission band. In particular, when the I_{exc} increased beyond 9.0 mW/μm^2, a series of new sharp emission lines with the average linewidth $\delta\lambda \sim 0.30$ nm started to emerge on the spontaneous emission spectra, whereas the emission band (380 nm) indicated little change in spectral shape at this stage. This indicates that optical resonance could be formed with specific modes in the ZnO@ZnO:Ga MW.

When $I_{exc} > 9.0$ mW/μm^2, the PL spectra are dominated by a series of sharp emission lines, together with more emission peaks that appeared with the increase in I_{exc}. The emission intensity of the single ZnO@ZnO:Ga MW demonstrated a dramatically superlinear increase versus I_{exc}, and the intensity is orders of magnitude greater than the spontaneous emission background, accompanied by the broad spontaneous emission

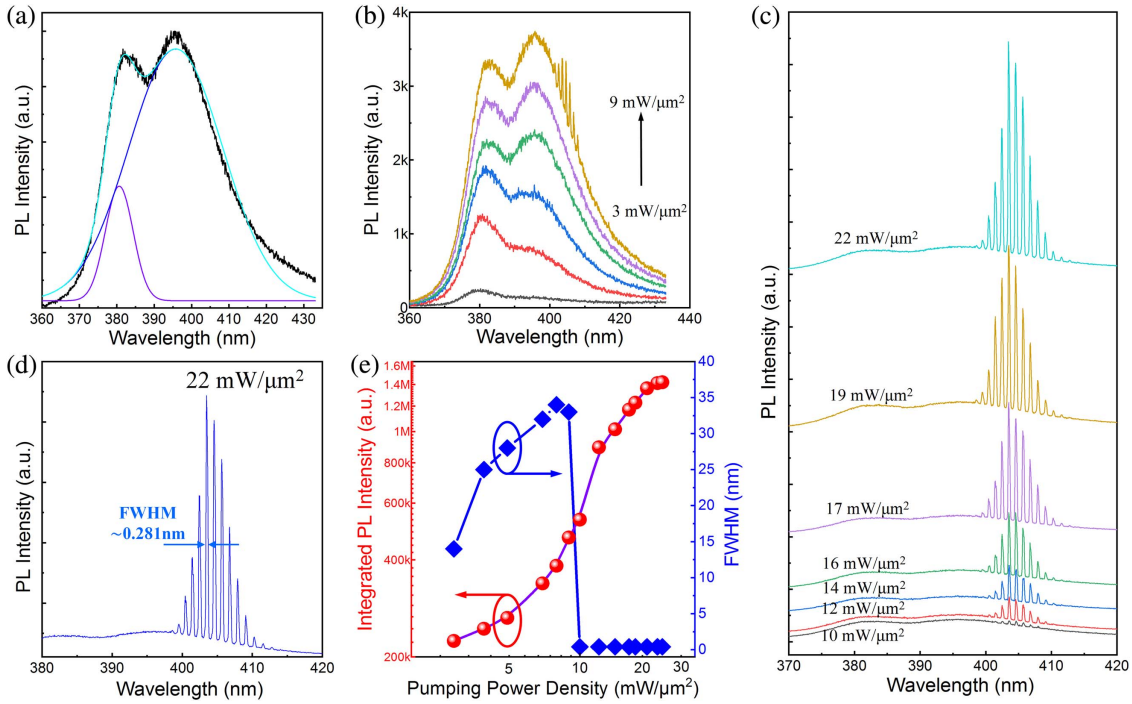

Fig. 3. Optically pumped lasing features from single ZnO@ZnO:Ga MW. (a) Two distinct Gaussian deconvoluted sub-bands of the PL spectrum from single ZnO@ZnO:Ga MW, with the excitation power density ~7.0 mW/μm². (b) Optically pumped emission spectra from single ZnO@ZnO:Ga MW, with the excitation power density ranging from 3.0 to 9.0 mW/μm². (c) Optically pumped emission spectra as a function of pumping intensity when the excitation power energies exceed 9.0 mW/μm². (d) The magnified lasing spectrum demonstrates that the FWHM of the lasing mode is about 0.06 nm (the excitation power density: 22.0 mW/μm²). (e) Nonlinear relationship between integrated emission intensities and the excitation power density, and FWHM versus the excitation power density. The lasing threshold was extracted to be about 9.0 mW/μm².

band being suppressed, as demonstrated in Fig. 3(c). This indicates that multi-mode lasing action can be generated from single ZnO@ZnO:Ga MW. One of the remarkable lasing features is that the lasing wavelengths of the whole emission band ranged from 398.5 to 413.0 nm, with the dominant wavelengths centered around 405.0 nm. It is also interesting to note that there is no shift of the dominant discrete peaks. Taking the $I_{exc} \sim 22.0$ mW/μm² as an example, the emission spectrum indicated that the average mode spacing was about 1.05 nm, the spectral linewidth $\delta\lambda$ for a single sharp emission peak was about 0.281 nm, and it could be estimated that the Q factor of this microcavity was about 1500 according to the equation $Q = \lambda/\delta\lambda$, where λ and $\delta\lambda$ are the lasing wavelength and its spectral linewidth, respectively, as shown in Fig. 3(d). This suggests that an evolvement process from spontaneous emission to stimulated emission can occur [8,31,35].

As previously reported, low-dimensional semiconducting structures with quadrilateral cross section were used to construct F–P mode microcavities [30,36]. Taking single MW with quadrilateral cross section as an example, optically pumped F–P mode lasing was realized, accompanied by bilateral sides that served as the optical feedback mirrors. To confirm that the lasing behavior from optically pumped single ZnO@ZnO:Ga MW can also be ascribed to the F–P mode resonant cavity, the mode spacing $\Delta\lambda$ versus the optical cavity length L could be calculated by the following formula: $\Delta\lambda = \lambda^2/[2L(n - \lambda dn/d\lambda)]$, where n is the relative refractive index ~2.5, the $dn/d\lambda$ is the Sellmeier first-order dispersion relation ($dn/d\lambda$ is −0.015 nm^{-1} at 405 nm), and the cavity length L was calculated to be about 10 μm, which is consistent with the experimentally observed width of the MW. Compared with the conventional F–P mode optical cavity, the quadrate-shaped cross section can provide a cavity resonator in which the emitted photon would be continuously amplified by stimulated emission while traveling back and forth, triggering a lasing emission [8,30,31,36].

To shed more light on the F–P mode lasing features, Fig. 3(e) shows the integrated emission intensity versus I_{exc}. The input-output curve agreed well with the Casperson model for multi-mode lasing, with the threshold excitation power energy $I_{exc} \sim 9.0$ mW/μm² estimated as the lasing threshold. When the $I_{exc} > 9.0$ mW/μm², a series of resonance peaks were selectively and strongly amplified. Above the onset power, the spectral linewidth dramatically narrowed down to about 0.3 nm, indicating an identifiable knee behavior and a threshold characteristic of a laser. In addition, increasing the excitation energy density, the dominant discrete peaks of the F–P mode lasing band exhibited little shift as well as no significant change of the spectral linewidth. By comparing optically pumped lasing behaviors from single ZnO MC and ZnO:Ga MWs, the violet lasing band from optically pumped single ZnO@ZnO:Ga MW cannot be attributed to an electron-hole

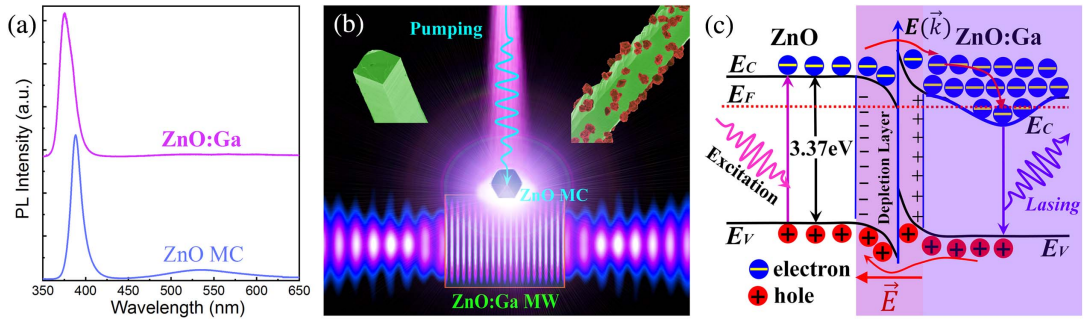

Fig. 4. Working principle of optically pumped F–P mode lasing action from single ZnO@ZnO:Ga MW. (a) Comparison of normalized PL spectra from single ZnO MC and single ZnO:Ga MW. (b) Schematic illustration of optically pumped F–P mode microsized laser composed of single ZnO@ZnO:Ga MW. (c) Energy-band alignment toward the homointerface between ZnO MC and ZnO:Ga MW.

plasma effect, even if operated under higher excitation energy density [31,35,40].

By comparison, PL emissions showed that the dominating emission peak centered at 378 nm was recorded from single ZnO:Ga MW, whereas the dominating emission peak of ZnO MC centered at 388 nm, as demonstrated in Fig. 4(a). Thus, the violet lasing emission band from single ZnO@ZnO:Ga MW cannot be attributed to ZnO MC or the pre-synthesized ZnO:Ga MW. On the contrary, the emissions may originate from the interfacial radiative recombination between ZnO MC and ZnO:Ga MW. To exploit the intrinsic lighting mechanism, the generated photons can be confined within the ZnO:Ga MW with quadrilateral cross section, with both bilateral sides serving as F–P mode reflecting mirrors. Thereby, the emitted photons may be amplified such that the lighting wave can travel back and forth between both bilateral sides at crystal boundaries between ZnO and air coherently, making the light signal waveguiding and oscillating more efficiently at room temperature, as shown in Fig. 4(b). In general, optically pumped lasing features from the semiconducting structures may be determined by many uncertain factors, such as the optical gain medium, high-quality optical microcavities, and surface modification. Therefore, the deposition of ZnO MCs on the pre-synthesized ZnO:Ga MW can be used to modulate the optical microcavity quality [25,41,42].

The built-in potential may be formed at any type of interface between dissimilar materials, and it could be employed to determine many fundamental characteristics in surface or interfacial sciences, such as electrode potentials, Schottky barriers, work functions, redox potentials, and energy-band offsets [43–46]. Specifically, it is crucial to the understanding of many interfacial features because it dominates the band alignment at the interface. Regarding the type-II energy-band alignment, the minimum of the conduction band and the maximum of the valence band can locate in different semiconductors. As a consequence, the photoexcited carriers are separated from each other spatially. After relaxation, indirectly radiative recombination can occur, with their emission spectra indicating unusual dependence on the excitation power intensity [12,20,47]. Herein, the contact-potential barrier formed between ZnO MC and ZnO:Ga MW may be ascribed to the following factors: (i) due to Ga incorporation, electron concentration on the order of 10^{19} cm^{-3} can be roughly estimated from the resistivity values, leading to the improvement of electronic transport of the bare MW [29,38]; (ii) because ZnO and ZnO:Ga are n-type semiconductors, an $n–n^+$ junction can be formed toward the heterointerface [48]; and (iii) finally, the Ga incorporation can drive excess electrons to occupy the conduction band of ZnO:Ga, resulting in the Burstein–Moss effect [29,37]. The electron filling induced the upshift of the Fermi level into the conduction band of ZnO:Ga, which can be responsible for the blueshift of typical NBE emission [37,39]. Due to the single ZnO@ZnO:Ga MW, energy-band alignment can occur, and the position of the conduction band in ZnO is higher than that of ZnO:Ga. Because the electron concentration in ZnO:Ga is about 3 orders of magnitude greater than the electron concentration in ZnO, the electron injection from ZnO into ZnO:Ga is dominant over the hole injection from ZnO into ZnO:Ga, leading to the diffusion of electrons and holes between ZnO MC and ZnO:Ga MW. Built-in electric field allows the electrons and holes to move in the opposite direction, as indicated in Fig. 4(c) [47,49–51].

The intrinsic lighting mechanism of the violet F–P mode lasing behavior from single ZnO@ZnO:Ga MW was investigated, and is interpreted as follows. Under lasing illumination, photoexcited carriers from the single ZnO@ZnO:Ga MW were generated. Driven by the built-in electric field, the light-induced electrons would flow from the conduction band of ZnO MC to the conduction band of ZnO:Ga, whereas the photoexcited holes migrate toward the valence band of ZnO:Ga and are then trapped in ZnO:Ga near the ZnO/ZnO:Ga interfacial region. Accordingly, the emitted photons could be collected from radiative recombination, located toward the interfacial depletion region between ZnO MC and ZnO:Ga MW. Compared with PL emissions from single ZnO MC and ZnO:Ga MW, the typical redshift of the violet lasing emission band from single ZnO@ZnO:Ga MW could be attributed to the bandgap renormalization, which causes a downshift of the conduction-band edge and an upshift of the valence-band edge. That is, optically pumped violet F–P mode lasing from single ZnO@ZnO:Ga MW can be attributed to type-II band alignment [35,41,52].

D. Electrical Injection Exciton-Polariton Diode Based on Single ZnO@ZnO:Ga MW

To further illustrate the influence of ZnO MCs on the well-crystallized ZnO:Ga MWs with quadrilateral cross section, single ZnO@ZnO:Ga MW was selected to fabricate a heterostructured light-emission device, with GaN substrate as the hole injection layer. By applying a forward injection current at room temperature, blue-ultraviolet light emission can be seen clearly with the naked eye, as shown in Fig. 5. Under lower injection current, such as 5.5 mA, bright blue lighting was captured from the heterostructured light-emitting device. Increasing the injection current to 12.0 mA, the optical characterization of bright ultraviolet lighting was also collected from the single ZnO@ZnO:Ga MW-based heterostructured emission device. Meanwhile, the bright emission regions distributed along both bilateral sides of the MW indicated that the emitted photons can be confined in the bilateral sides of the synthesized MW. Remarkably, by increasing the injection current, the blue-violet lighting demonstrated a clear blueshift tendency, which may be induced by the energy-band broadening. Additionally, the lighting phenomenon represented interrupted and uneven brightness, with the dark regions possibly caused by the local poor contact due to uneven pressure exerted between the ZnO@ZnO:Ga MW and the p-GaN layer.

To probe the emission characteristics, electronic transport properties and the light-emission features of single ZnO@ZnO:Ga MW-based heterojunction diode were taken into account. Figure 6(a) demonstrates the I–V curve, indicating typical rectification characteristics with the turn-on voltage being about 3.4 V. Additionally, the light emitted from the heterojunction diode was also collected. Figure 6(b) reveals the EL emission spectra with the injection current ranging from 0.005 to 12.5 mA. The dominating emission peaks centered at 405 nm, accompanied by negligible visible emissions. With an increase of the injection current, a small blueshift of the dominating emission peaks can be recorded. Furthermore, the integrated emission intensities increased as an approximately linear relationship versus the injection current, suggesting the spontaneous emission behavior, as indicated in Fig. 6(c). In addition, the spectral linewidth versus the injection current was also studied and revealed that there was little change in the spectral linewidth of the emission packet [see Fig. 6(c)].

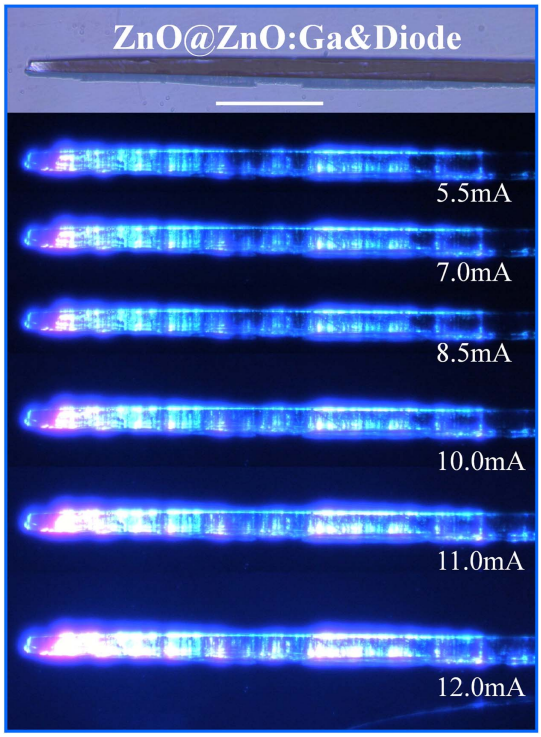

Fig. 5. Optical microscopic image of the light emitting from electrically biased single ZnO@ZnO:Ga MW-based heterojunction diode. With an increase in the injection current ranging from 5.5 to 12.0 mA, bright and blue-violet light emission can be observed, with the lighting regions located along the MW.

The EL spectra exhibited periodic multi-peak characteristics. Due to the waveguiding spectra and optical microscopic images, it could be deduced that bilateral facets of the MWs could serve as optical feedback mirrors, employed to construct the laser cavities naturally [28,30,36]. Therefore, single ZnO@ZnO:Ga MW with quadrilateral cross section can function as well-defined optical waveguide. Taking the EL emission spectrum (injection current: 12.5 mA), for instance, the multi-peak spectrum demonstrated a pronounced modulation across the ultraviolet-to-blue spectral band, with the mode spacing of the emission peaks increasing slightly in the longer wavelength region ranging from 4.5 to 7.5 nm, suggesting that single ZnO@ZnO:Ga MW can function as a high-quality optical microcavity. The recorded multi-peak emission features may be attributed to the typical cavity modes. In addition, one can also see that the energy spacing between neighboring modes is becoming smaller with the energy shifting toward the exciton resonance. Because the energies of the optical modes in the ultraviolet region are close to those of the excitons, the strong interaction between these optical modes and excitons was expected, and the exciton-polariton effect should be included for proper understanding of the ultraviolet EL emission spectra of single ZnO@ZnO:Ga MW-based heterojunction diode [53–56].

When the injection current was beyond 2.0 mA, the central emission wavelength of the heterojunction diode was in accordance with the dominant lasing peak of single ZnO@ZnO:Ga MW. Thus, the injected electrons could be confined and accumulated in the ZnO@ZnO:Ga MW. Meanwhile, the holes could also be injected into the MW. Therefore, typical excitonic emission was achieved on account of single ZnO@ZnO:Ga MW-based heterojunction diode [30,37,57,58]. The oscillating modes may be interpreted using exciton-polariton quasi-particle behavior. Consequently, the recorded series of resonance peaks on the EL spectrum can be attributed to the exciton-polariton lighting feature. Taking the EL spectrum indicated in Fig. 6(d) as an example, where the well-defined quadrilateral cross section of ZnO@ZnO:Ga MW functioned as the F–P optical cavity, the cavity length L can be calculated by the formula $\delta\lambda \approx \lambda^2/2nL$, where n is the refractive index ($n = 2.5$ for ZnO@ZnO:Ga), λ is the resonant wavelength, and $\delta\lambda$ is the mode spacing. The calculated cavity length is about 5 μm, which is much smaller than the measured width of the synthesized ZnO@ZnO:Ga MW. It could be deduced

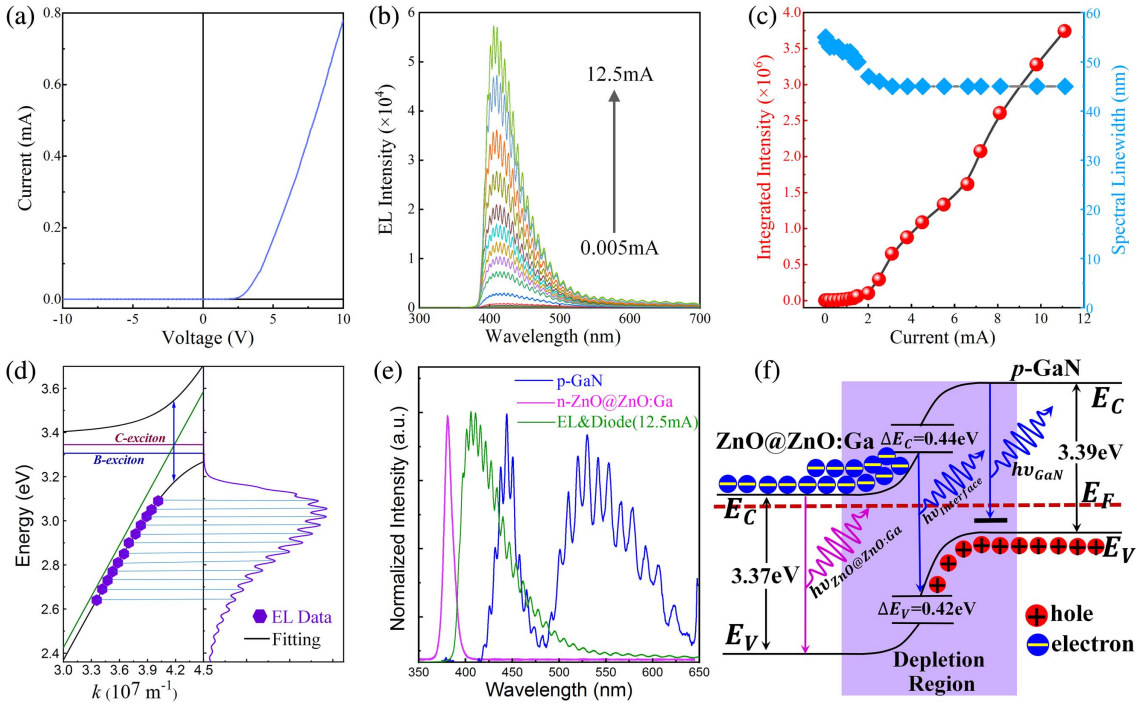

Fig. 6. Exciton-polariton emission characteristics from electrical-pumping single ZnO@ZnO:Ga MW-based heterojunction diode. (a) I–V characteristics curve from single ZnO@ZnO:Ga MW-based heterojunction diode. (b) Electrical-pumping emission spectra from single ZnO@ZnO:Ga MW-based heterojunction diode, with the injection current ranging from 0.005 to 12.5 mA. (c) Linear relationship between integrated emission intensity and the injection current, together with the spectral linewidth versus the injection current. (d) Energy-wavevector dispersion curve of single ZnO@ZnO:Ga MW-based heterojunction diode. (e) Normalized emission spectra of the PL emission from single ZnO@ZnO:Ga MW, PL emission from p-GaN layer, and EL emission spectrum from the heterojunction diode composed of single ZnO@ZnO:Ga MW and p-GaN layer. (f) Schematic diagram showing the energy-band alignment of the n-ZnO@ZnO:Ga/p-GaN heterojunction diode.

that the bilateral sides of the MWs could not serve as optical feedback mirrors and are more apt to be employed to support waveguided channel for the emitted photons. Therefore, single ZnO@ZnO:Ga MW with quadrilateral cross section can function as well-defined waveguide [28,54,59,60].

ZnO-based micro-/nanostructures with highly smooth surface and well-defined crystal boundary have been employed to exploit polariton lasing characteristics. The investigation of strong coupling between excitons and photons and the relationship between coupling strength and lasing threshold has motivated us not only to construct ultralow threshold coherent light sources and model systems for polaritonics but also to gain a better understanding of this class of materials in optoelectronics applications [1,27,54,61]. Because of the single MW with quadrilateral cross section, the exciton-polariton dispersion relation can be expressed as follows [52–54,56]:

$$E(\omega,\vec{k}) = \hbar\omega(\vec{k}) = \frac{\hbar c\vec{k}}{\sqrt{\varepsilon_b\left(1+\frac{\omega_L^2-\omega_T^2}{\omega_T^2-\omega^2-i\omega\gamma}\right)}}, \tag{1}$$

where ε_b is the background dielectric constant and ω_L and ω_T are the longitudinal and transverse resonance frequencies of the excitons, respectively. According to Eq. (1), the energy levels of a propagating exciton-polariton could be divided into the upper and lower branches versus wave vector $\vec{k}$. Meanwhile, the refractive index and the polariton dispersion in ZnO@ZnO:Ga MWs can be well described by the coupling oscillator model in the simple dielectric approximation formula:

$$n^2 = \varepsilon(\omega,k) = \varepsilon_b\left[1+\sum_{i=A,B,C}\frac{\Omega_i(\omega_{i,L}^2-\omega_{i,T}^2)}{\omega_{i,T}^2-\omega^2-i\omega\Gamma_i}\right] = \frac{c^2k^2}{\omega^2}, \tag{2}$$

where n is the refractive index, ε_b is the background dielectric constant, $\omega_{i,T}$ and $\omega_{i,L}$ are the transverse and longitudinal resonance frequencies, respectively, and Γ_i is the damping constant [52,53,56,60]. Therefore, the dispersion relationship curves can be separated into an upper exciton-polariton branch and a lower exciton-polariton branch, with the energy gap between these two branches being approximately identified as Rabi splitting. Energy-wavevector dispersion curves of single ZnO@ZnO:Ga MW-based heterojunction diode could be described, as demonstrated in Fig. 6(d). The generated photons and excitons energies dispersion relation, confined in the quasi-quadrilateral ZnO@ZnO:Ga MW, was also indicated. To exploit the exciton-polariton dispersion relationship, the dominant emission peaks were extracted from the EL spectrum [Fig. 6(d)]. Additionally, the absence of the upper polariton branch is expected as a result of the strong absorption in the scattering and continuum states of ZnO@ZnO:Ga MW

excitons, together with the polariton thermalization, especially in the system with a large normal mode splitting. The Rabi splitting between the polariton branches is as high as 400 meV, which was acquired as the exciton binding energy of the as-synthesized ZnO@ZnO:Ga MW. It can be confirmed that the experimental results were coincide well with the exciton-polariton dispersion curves, which derived from the strong coupling between the optical F–P modes and excitons [41,53,54,61].

By comparison, PL emission signals of the single ZnO@ZnO:Ga MW and p-GaN layer were recorded under the same excitation condition, as demonstrated in Fig. 6(e). The dominating PL emission peak of ZnO@ZnO:Ga MW centered around 390 nm. The PL spectrum of the p-GaN layer was characterized by a broad blue emission peak centered at 443.5 nm, accompanied by a broad visible emission band centered at 530 nm. The PL emissions could be attributed to the transition from the conduction band, together with the unidentified shallow donors to deep Mg-related acceptor levels. Therefore, the broad EL spectra could be decomposed of three distinct subbands: (i) NBE-type emission of ZnO@ZnO:Ga MW; (ii) the lighting in the blue spectral band can be ascribed to the transitions from the conduction band or unidentified shallow donors to Mg-acceptor levels of the p-GaN layer; and (iii) the lighting centered around 425 nm can be attributed to the interfacial radiative recombination of the electrons from n-ZnO@ZnO:Ga MW and holes from the p-GaN layer, with the junction depletion region located toward the interfacial region between ZnO@ZnO:Ga MW and p-GaN layer [28,30,57,58].

To further investigate the electrically driven lighting mechanism, the energy band diagram of single ZnO@ZnO:Ga MW-based heterojunction diodes was depicted. First, at a lower injection current, the EL spectra showed that the dominating emission peaks centered around 420 nm could be attributed to interfacial emissions, which formed at the n-ZnO@ZnO:Ga/p-GaN heterointerface. Meanwhile, the spectral linewidth, ~45 nm, was much wider than that of the PL spectrum from single ZnO@ZnO:Ga MW. Thus, an energy barrier was formed toward the n-ZnO@ZnO:Ga/p-GaN interface, which is likely caused by the fabrication process. The barriers at the interface for the holes and the electrons are approximately equal. At a lower injection current, the broad EL emission band from the heterojunction diode was derived from the emissions from the ZnO@ZnO:Ga MW and p-GaN as well as hetero-interfacial lighting [53,57,58]. In contrast, PL emission of single ZnO@ZnO:Ga MW was attributed to typical NBE recombination, whereas the emission centered at 450 nm was assigned to Mg-related deep acceptor levels in the p-GaN layer. Thus, the emission centered at 420 nm can be attributed to the interfacial radiative recombination of the electrons from n-ZnO:Ga, accompanied by holes originating from p-GaN. The barrier heights toward the interface for the holes and the electrons could be calculated to be 0.42 eV and 0.44 eV, respectively. The energy band diagram under a lower injection current is shown in Fig. 6(f). With an increase in the injection current, the dominant EL emissions turned into typical NBE emission of ZnO@ZnO:Ga MW, accompanied by the efficient suppression of the interfacial emissions. The energy-band alignment of a single ZnO/ZnO:Ga MW-based heterojunction diode can be engineered, together with the efficient carrier injection and excitonic-type recombination EL development, because of the as-synthesized single MW.

4. CONCLUSIONS

In summary, ZnO MCs as well as individual ZnO:Ga MWs covered with ZnO MCs have been successfully synthesized. Because of the advantages of highly smooth surfaces and well-defined grain boundaries, single ZnO MCs can be used to construct optically pumped random microsized lasers. In particular, optically pumped violet F–P mode lasing was achieved from single ZnO@ZnO:Ga MW, with the lasing band covering from 398.5 to 413 nm. The redshift of the lasing band, together with the dominating lasing peak centered around 405 nm, can be attributed to a conduction band offset between ZnO MC and ZnO:Ga MW, yielding a type-II transition. To anticipate the potential application, single ZnO@ZnO:Ga MW featuring a well-defined quadrilateral cross section was selected to construct a heterojunction diode. Multi-peak emissions were captured in the blue-ultraviolet spectral region, which can be attributed to an exciton-polariton effect. These experimental findings are attractive because they can open the approach toward practical applications, such as polariton emitters and lasers and exciton-polariton photonic and optoelectronic devices.

Funding. National Natural Science Foundation of China (11574307, 11974182, U1604263, 11774171, 21805137, 11874220); Priority Academic Program Development of Jiangsu Higher Education Institutions (KYZZ16-0164).

Disclosures. The authors declare that there are no conflicts of interest related to this paper.

REFERENCES

1. Y. Peng, W. Lu, P. Ren, Y. Ni, Y. Wang, L. Zhang, Y.-J. Zeng, W. Zhang, and S. Ruan, "Integration of nanoscale light emitters: an efficient ultraviolet and blue random lasing from $NAYF_4$:Yb/Tm hexagonal nanocrystals," Photon. Res. **6**, 943–947 (2018).
2. D. J. Garfield, N. J. Borys, S. M. Hamed, N. A. Torquato, C. A. Tajon, B. Tian, B. Shevitski, E. S. Barnard, Y. D. Suh, S. Aloni, J. B. Neaton, E. M. Chan, B. E. Cohen, and P. J. Schuck, "Enrichment of molecular antenna triplets amplifies upconverting nanoparticle emission," Nat. Photonics **12**, 402–407 (2018).
3. X. Liu, K. Mashooq, D. A. Laleyan, E. T. Reid, and Z. Mi, "Algan nanocrystals: building blocks for efficient ultraviolet optoelectronics," Photon. Res. **7**, B12–B23 (2019).
4. J. J. Cole, X. Wang, R. J. Knuesel, and H. O. Jacobs, "Integration of ZnO microcrystals with tailored dimensions forming light emitting diodes and UV photovoltaic cells," Nano Lett. **8**, 1477–1481 (2008).
5. H. Siampour, S. Kumar, V. A. Davydov, L. F. Kulikova, V. N. Agafonov, and S. I. Bozhevolnyi, "On-chip excitation of single germanium-vacancies in nanodiamonds embedded in plasmonic waveguides," Light Sci. Appl. **7**, 61 (2018).
6. Y. Wu, Z. Li, K.-W. Ang, Y. Jia, Z. Shi, Z. Huang, W. Yu, X. Sun, X. Liu, and D. Li, "Monolithic integration of MoS_2-based visible detectors and GaN-based UV detectors," Photon. Res. **7**, 1127–1133 (2019).
7. Y. Wang, X. Wang, B. Zhu, Z. Shi, J. Yuan, X. Gao, Y. Liu, X. Sun, D. Li, and H. Amano, "Full-duplex light communication with a monolithic multicomponent system," Light Sci. Appl. **7**, 83 (2018).

8. J. Tatebayashi, S. Kako, J. Ho, Y. Ota, S. Iwamoto, and Y. Arakawa, "Room-temperature lasing in a single nanowire with quantum dots," Nat. Photonics **9**, 501–505 (2015).
9. M. S. Gudiksen, L. J. Lauhon, J. Wang, D. C. Smith, and C. M. Lieber, "Growth of nanowire superlattice structures for nanoscale photonics and electronics," Nature **415**, 617–620 (2002).
10. P. Narayan, G. David, T. Jason, and X. Peng, "An alternative of CdSe nanocrystal emitters: pure and tunable impurity emissions in ZnSe nanocrystals," J. Am. Chem. Soc. **127**, 17586–17587 (2005).
11. Z. Xiao, R. A. Kerner, L. Zhao, N. L. Tran, K. M. Lee, T. W. Koh, G. D. Scholes, and B. P. Rand, "Efficient perovskite light-emitting diodes featuring nanometre-sized crystallites," Nat. Photonics **11**, 108–115 (2017).
12. T. Uchino and D. Okutsu, "Broadband laser emission from color centers inside MgO microcrystals," Phys. Rev. Lett. **101**, 117401 (2008).
13. R. Saran and R. J. Curry, "Lead sulphide nanocrystal photodetector technologies," Nat. Photonics **10**, 81–92 (2016).
14. X. Wang, J. Zhuang, Q. Peng, and Y. Li, "A general strategy for nanocrystal synthesis," Nature **437**, 121–124 (2005).
15. F. P. Garcia de Arquer, A. Armin, P. Meredith, and E. H. Sargent, "Corrigendum: solution-processed semiconductors for next-generation photodetectors," Nat. Rev. Mater. **2**, 16100 (2017).
16. I. Song, S. C. Lee, X. Shang, J. Ahn, H. J. Jung, C. U. Jeong, S. W. Kim, W. Yoon, H. Yun, and O. P. Kwon, "High-performance visible-blind UV phototransistors based on n-type naphthalene diimide nanomaterials," ACS Appl. Mater. Interface **10**, 11826–11836 (2018).
17. X. Zhang, J. Jie, W. Deng, Q. Shang, J. Wang, H. Wang, X. Chen, and X. Zhang, "Alignment and patterning of ordered small-molecule organic semiconductor micro-/nanocrystals for device applications," Adv. Mater. **28**, 2475–2503 (2016).
18. D. Sun, D. Yi, X. Tian, Z. Li, Z. Chen, and C. Zhu, "Microwave-assisted synthesis and optical properties of cuprous oxide micro/nanocrystals," Mater. Res. Bull. **60**, 704–708 (2014).
19. W. Cao, W. Du, F. Su, and G. Li, "Anti-Stokes photoluminescence in ZnO microcrystal," Appl. Phys. Lett. **89**, 031902 (2006).
20. H. Dong, Y. Wei, W. Zhang, C. Wei, C. Zhang, J. Yao, and Y. S. Zhao, "Broadband tunable microlasers based on controlled intramolecular charge-transfer process in organic supramolecular microcrystals," J. Am. Chem. Soc. **138**, 1118–1121 (2016).
21. B. Yang, H. Chen, X. Shuang, Q. Xue, Z. Teng, Z. Zhu, L. Qiang, H. Chen, Y. Yun, and Z. Hu, "Effects of a molecular monolayer modification of NiO nanocrystal layer surfaces on perovskite crystallization and interface contact toward faster hole extraction and higher photovoltaic performance," Adv. Funct. Mater. **26**, 2950–2958 (2016).
22. L. Korala, M. Braun, J. M. Kephart, Z. Tregillus, and A. L. Prieto, "Ligand-exchanged CZTS nanocrystal thin films: does nanocrystal surface passivation effectively improve photovoltaic performance?" Chem. Mater. **29**, 6621–6629 (2017).
23. X. Wang, H. Li, Y. Wu, Z. Xu, and H. Fu, "Tunable morphology of the self-assembled organic microcrystals for the efficient laser optical resonator by molecular modulation," J. Am. Chem. Soc. **136**, 16602–16608 (2014).
24. H. He, E. Ma, J. Yu, Y. Cui, Y. Lin, Y. Yang, X. Chen, B. Chen, and G. Qian, "Periodically aligned dye molecules integrated in a single MOF microcrystal exhibit single-mode linearly polarized lasing," Adv. Opt. Mater. **5**, 1601040 (2017).
25. J. W. Soares, J. E. Whitten, D. W. Oblas, and D. M. Steeves, "Novel photoluminescence properties of surface-modified nanocrystalline zinc oxide: toward a reactive scaffold," Langmuir **24**, 371–374 (2008).
26. Z. Wang, J. Christiansen, D. Wezendonk, X. Xie, M. A. van Huis, and A. Meijerink, "Thermal enhancement and quenching of upconversion emission in nanocrystals," Nanoscale **11**, 12188–12197 (2019).
27. O. Jamadi, F. Reveret, P. Disseix, F. Medard, J. Leymarie, A. Moreau, D. Solnyshkov, C. Deparis, M. Leroux, and J. Zuniga-Perez, "Edge-emitting polariton laser and amplifier based on a ZnO waveguide," Light Sci. Appl. **7**, 82 (2017).
28. M. Jiang, W. Mao, X. Zhou, C. Kan, and D. N. Shi, "Wavelength-tunable waveguide emissions from electrically driven single ZnO/ZnO:Ga superlattice microwires," ACS Appl. Mater. Interface **11**, 11800–11811 (2019).
29. M. Jiang, G. He, H. Chen, Z. Zhang, L. Zheng, C. Shan, D. Shen, and X. Fang, "Wavelength-tunable electroluminescent light sources from individual Ga-doped ZnO microwires," Small **13**, 1604034 (2017).
30. Z. Li, M. Jiang, Y. Sun, Z. Zhang, B. Li, H. Zhao, C. Shan, and D. Shen, "Electrically pumped Fabry–Perot microlasers from single Ga-doped ZnO microbelt based heterostructure diodes," Nanoscale **10**, 18774–18785 (2018).
31. C. Xu, J. Dai, G. Zhu, G. Zhu, L. Yi, J. Li, and Z. Shi, "Whispering gallery mode lasing in ZnO microcavities," Laser Photon. Rev. **8**, 469–494 (2014).
32. Y. Liu, M. Jiang, Z. Zhang, B. Li, H. Zhao, C. Shan, and D. Shen, "Electrically excited hot-electron dominated fluorescent emitters using individual Ga-doped ZnO microwires via metal quasiparticle film decoration," Nanoscale **10**, 5678–5688 (2018).
33. W. Peng, S. Qu, G. Cong, and Z. Wang, "Synthesis and structures of morphology-controlled ZnO nano- and microcrystals," Cryst. Growth Des. **6**, 1518–1522 (2006).
34. Z. Li, F. Xu, X. Sun, and W. Zhang, "Oriented attachment in vapor: formation of ZnO three-dimensional structures by intergrowth of ZnO microcrystals," Cryst. Growth Des. **8**, 805–807 (2008).
35. J. Dai, C. Xu, T. Nakamura, Y. Wang, J. Li, and Y. Lin, "Electron-hole plasma induced band gap renormalization in ZnO microlaser cavities," Opt. Express **22**, 28831–28837 (2014).
36. M. Ding, D. Zhao, B. Yao, E. Shulin, Z. Guo, L. Zhang, and D. Shen, "The ultraviolet laser from individual ZnO microwire with quadrate cross section," Opt. Express **20**, 13657–13662 (2012).
37. Y. Liu, M. Jiang, G. He, S. Li, Z. Zhang, B. Li, H. Zhao, C. Shan, and D. Z. Shen, "Wavelength-tunable ultraviolet electroluminescence from Ga-doped ZnO microwires," ACS Appl. Mater. Interface **9**, 40743–40751 (2017).
38. G. D. Yuan, W. J. Zhang, J. S. Jie, X. Fan, J. X. Tang, I. Shafiq, Z. Z. Ye, C. S. Lee, and S. T. Lee, "Tunable n-type conductivity and transport properties of Ga-doped ZnO nanowire arrays," Adv. Mater. **20**, 168–173 (2010).
39. W. T. Ruane, K. M. Johansen, K. D. Leedy, D. C. Look, W. H. Von, M. Grundmann, G. C. Farlow, and L. J. Brillson, "Defect segregation and optical emission in ZnO nano- and microwires," Nanoscale **8**, 7631–7637 (2016).
40. T. Nakamura, K. Firdaus, and S. Adachi, "Electron-hole plasma lasing in a ZnO random laser," Phys. Rev. B **86**, 205103 (2012).
41. R. Chen, Q. L. Ye, T. He, V. D. Ta, Y. Ying, Y. Y. Tay, T. Wu, and H. Sun, "Exciton localization and optical properties improvement in nanocrystal-embedded ZnO core–shell nanowires," Nano Lett. **13**, 734–739 (2013).
42. D. Mrinal, T. Lavanya, T. Pham Van, and F. Naoki, "High efficiency hybrid solar cells using nanocrystalline Si quantum dots and Si nanowires," ACS Nano **9**, 6891–6899 (2015).
43. M.-P. Zhuo, X.-Y. Fei, Y.-C. Tao, J. Fan, X.-D. Wang, W.-F. Xie, and L.-S. Liao, "*In situ* construction of one-dimensional component-interchange organic core/shell microrods for multicolor continuous-variable optical waveguide," ACS Appl. Mater. Interface **11**, 5298–5305 (2019).
44. B. Zhao, S. Bai, V. Kim, R. Lamboll, R. Shivanna, F. Auras, J. M. Richter, L. Yang, L. Dai, M. Alsari, X.-J. She, L. Liang, J. Zhang, S. Lilliu, P. Gao, H. J. Snaith, J. Wang, N. C. Greenham, R. H. Friend, and D. Di, "High-efficiency perovskite-polymer bulk heterostructure light-emitting diodes," Nat. Photonics **12**, 783–789 (2018).
45. H. Dong, C. Zhang, Y. Liu, Y. Yan, F. Hu, and Y. S. Zhao, "Organic microcrystal vibronic lasers with full-spectrum tunable output beyond the Franck–Condon principle," Angew. Chem. **130**, 3162–3166 (2018).
46. H. Wang, J. Wen, W. Wang, N. Xu, P. Liu, J. Yan, H. Chen, and S. Deng, "Resonance coupling in heterostructures composed of silicon nanosphere and monolayer WS_2: a magnetic-dipole-mediated energy transfer process," ACS Nano **13**, 1739–1750 (2019).
47. F. Di Stasio, A. Polovitsyn, I. Angeloni, I. Moreels, and R. Krahne, "Broadband amplified spontaneous emission and random lasing from wurtzite CdSe/CdS 'giant-shell' nanocrystals," ACS Photon. **3**, 2083–2088 (2016).

48. B. Zhao, F. Wang, H. Chen, Y. Wang, M. Jiang, X. Fang, and D. Zhao, "Solar-blind avalanche photodetector based on single ZnO-Ga_2O_3 core–shell microwire," Nano Lett. **15**, 3988–3993 (2015).
49. Z. Chen, S. Berciaud, C. Nuckolls, T. F. Heinz, and L. E. Brus, "Energy transfer from individual semiconductor nanocrystals to graphene," ACS Nano **4**, 2964–2968 (2010).
50. R. Begum, M. R. Parida, A. L. Abdelhady, B. Murali, N. M. Alyami, G. H. Ahmed, M. N. Hedhili, O. M. Bakr, and O. F. Mohammed, "Engineering interfacial charge transfer in $CsPbBr_3$ perovskite nanocrystals by heterovalent doping," J. Am. Chem. Soc. **139**, 731–737 (2016).
51. S. Kreinberg, W. W. Chow, J. Wolters, C. Schneider, C. Gies, F. Jahnke, S. Hofling, M. Kamp, and S. Reitzenstein, "Emission from quantum-dot high-β microcavities: transition from spontaneous emission to lasing and the effects of superradiant emitter coupling," Light Sci. Appl. **6**, e17030 (2017).
52. D. Vanmaekelbergh and L. K. van Vugt, "ZnO nanowire lasers," Nanoscale **3**, 2783–2800 (2011).
53. Z. Zhang, Y. Wang, S. Yin, T. Hu, Y. Wang, L. Liao, S. Luo, J. Wang, X. Zhang, P. Ni, X. Shen, C. Shan, and Z. Chen, "Exciton-polariton light-emitting diode based on a ZnO microwire," Opt. Express **25**, 17375–17381 (2017).
54. W. Du, S. Zhang, J. Shi, J. Chen, Z. Wu, Y. Mi, Z. Liu, Y. Li, X. Sui, and T. Wu, "Strong exciton-photon coupling and lasing behavior in all-inorganic $CsPbBr_3$ micro/nanowire Fabry–Perot cavity," ACS Photon. **5**, 2051–2059 (2018).
55. J. Lagois, "Depth-dependent eigenenergies and damping of excitonic polaritons near a semiconductor surface," Phys. Rev. B **23**, 5511–5520 (1981).
56. L. Sun, Z. Chen, Q. Ren, K. Yu, L. Bai, W. Zhou, H. Xiong, Z. Q. Zhu, and X. Shen, "Direct observation of whispering gallery mode polaritons and their dispersion in a ZnO tapered microcavity," Phys. Rev. Lett. **100**, 156403 (2008).
57. A. Chen, H. Zhu, Y. Wu, G. Lou, Y. Liang, J. Li, Z. Chen, Y. Ren, X. Gui, S. Wang, and Z. Tang, "Electrically driven single microwire-based heterojuction light-emitting devices," ACS Photon. **4**, 1286–1291 (2017).
58. J. Dai, C. X. Xu, and X. W. Sun, "ZnO-microrod/p-gan heterostructured whispering-gallery-mode microlaser diodes," Adv. Mater. **23**, 4115–4119 (2011).
59. Y. Lai, Y. Lan, and T. Lu, "Strong light-matter interaction in ZnO microcavities," Light Sci. Appl. **2**, e76 (2013).
60. L. Sun, H. Dong, W. Xie, Z. An, X. Shen, and Z. Chen, "Quasi-whispering gallery modes of exciton-polaritons in a ZnO microrod," Opt. Express **18**, 15371–15376 (2010).
61. S. Zhang, Q. Shang, W. Du, J. Shi, Z. Wu, Y. Mi, J. Chen, F. Liu, Y. Li, M. Liu, Q. Zhang, and X. Liu, "Strong exciton-photon coupling in hybrid inorganic–organic perovskite micro/nanowires," Adv. Opt. Mater. **6**, 1701032 (2018).